nature astronomy

Article

https://doi.org/10.1038/s41550-024-02461-y

# Direct imaging of active galactic nucleus outflows and their origin with the 23 m Large Binocular Telescope

Received: 17 April 2024

Accepted: 29 November 2024

Published online: 17 January 2025

Check for updates

J. W. Isbell[1,2] ✉, S. Ertel[1,3], J.-U. Pott[2], G. Weigelt[4], M. Stalevski[5,6], J. Leftley[7], W. Jaffe[8], R. G. Petrov[7], N. Moszczynski[9], P. Vermot[9], P. Hinz[10], L. Burtscher[11], V. Gámez Rosas[8], A. Becker[3], J. Carlson[3], V. Faramaz-Gorka[1], W. F. Hoffmann[1], J. Leisenring[1], J. Power[3] & K. Wagner[1]

Active galactic nuclei (AGNs) are a key component of galaxy evolution owing to feedback on the host from its supermassive black hole. The morphology of warm inflowing and outflowing dusty material can reveal the nature of the onset of feedback, AGN feeding and the unified model of AGN. Here we use the Large Binocular Telescope Interferometer (LBTI) to image the dense, obscuring disk and extended dusty outflow region of NGC 1068. In Fizeau imaging mode, the LBTI synthesizes the equivalent resolution of a 22.8 m telescope. The 8.7 μm Fizeau images of NGC 1068 have an effective resolution of 47 × 90 mas (3.3 × 6.2 pc) in a 5″ field of view after performing point spread function deconvolution techniques described here. This is the only extragalactic source to be Fizeau imaged using the LBTI, and the images bridge the scales measured with the Very Large Telescope Interferometer (0.5–5 pc) and those of single telescopes such as James Webb Space Telescope and Keck (>15 pc). The images detect and spatially resolve the low surface brightness mid-infrared features in the AGN disk/wind region that are overresolved by the Very Large Telescope Interferometer. The images show strong correlation between mid-infrared dust emission and near-infrared emission of highly excited atomic lines observed by SINFONI. Such LBTI imaging is a precursor to infrared imaging using the upcoming generation of extremely large telescopes, with angular resolutions up to six times better than James Webb Space Telescope, the largest space telescope in orbit.

The study of active galactic nuclei (AGNs) at high spatial resolution aims to test the unified model of AGN[1], understand the AGN lifecycle and resolve the onset of AGN feedback—crucial information for studies of AGN at high redshift and within cosmological simulations. Dusty outflows are of particular interest because they dominate the energy budget of AGN feedback, especially in highly accreting AGN (for example, quasars)[2]. The winds are thought to be driven by radiation pressure from high-energy photons in the vicinity of the supermassive black hole (SMBH) (for example, refs. 3–7). In simulations, anisotropic radiation from the accretion disk[8] drives the dust primarily in the polar direction, but the outflows are further impacted by and impact inflowing material in a so-called fountain flow[3]. Polar extended dust has been commonly observed on parsec scales in a number of AGN with Very Large Telescope Interferometer (VLTI)/MIDI (MID-infrared interferometric instrument)[9,10] and studied more extensively in two nearby AGNs with VLTI/MATISSE (Multi AperTure mid-Infrared SpectroScopic

A full list of affiliations appears at the end of the paper. ✉e-mail: jwisbell@arizona.edu

https://doi.org/10.1038/s41550-024-02461-y

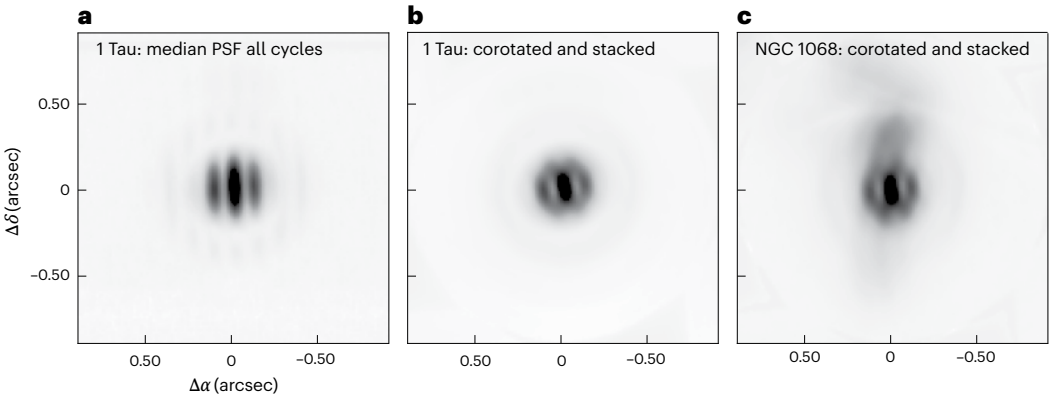


**Fig. 1 | Empirical PSF estimates. a**, The median PSF of 1 Tau throughout the night. **b**, The median PSF of 1 Tau stacked and rotated to match the NGC 1068 field rotation. This serves as an estimate of the empirical PSF of the corotated and stacked science image. **c**, Stacked and corotated Fizeau image of NGC 1068 combining the 20 nodding cycles. In all panels, north is up and east is left.

Experiment)[11–13]. However, how the AGN and its winds are fuelled and how the polar ejected material interacts with the host galaxy remain open questions.

NGC 1068 is an important laboratory for the understanding of AGN feeding and feedback. Located only 14.4 Mpc away, it is the prototypical Seyfert 2 AGN[1]; it led to the development of the unified AGN model. Its proximity and brightness have enabled extremely high-spatial-resolution imaging of its nucleus in the near-infrared (NIR)[14], mid-infrared (MIR)[13], submillimetre[15–17] and radio[18,19]. The submillimetre observations probe cold dust and dense molecular gas on similar scales as the Large Binocular Telescope Interferometer (LBTI). Interpretation of the connections between dusty, molecular material, hot ionized outflows and the AGN itself is complicated by interactions with the 'bent' radio jet[20], which leaves the core oriented approximately north–south, but is seen at large scales to be oriented northeast–southwest (for example, refs. 19). In addition, high-resolution NIR/MIR imaging at the VLTI with the 8.1 m unit telescopes resolves out structures larger than ~4 pc at 8.7 μm, so the link between the small-scale and galactic structures is tenuous. Measurements on scales intermediate to the existing 8.1 m single-dish observations and the 34 m VLTI shortest unit telescope baseline are necessary to understand how material is delivered to the accretion disk and to the nascent outflows.

The LBTI[21,22] co-phases and interferometrically combines the beams from the two 8.4 m mirrors of the Large Binocular Telescope (LBT), separated 14.4 m. In Fizeau imaging, this results in a virtual telescope aperture with a maximum baseline of 22.8 m. Although the auxiliary telescopes at the VLTI offer similar baselines, their 1.8 m diameters provide limited sensitivity compared with the LBTI. The LBTI thus provides complementary data to the existing VLTI observations of NGC 1068. Open-phase loop Fizeau interferometric imaging is the simplest interferometric mode of the LBTI. It has great potential for the high-fidelity, wide-field (~5 arcsec), intermediate-contrast imaging of faint NIR or MIR targets or targets that are too extended for phase tracking (examples include Solar System bodies, AGNs, ultraluminous infrared galaxies, and massive and evolved stars). The mode, however, has not been actively developed since its successful observations of Io[23–25]. Open-loop Fizeau imaging at the LBTI is poised to bridge the gap between high-dynamic-range single-dish observations with, for example, James Webb Space Telescope (JWST), and low-dynamic-range high-resolution interferometric images with, for example, VLTI and the Center for High Angular Resolution Astronomy (CHARA). Its 22.8 m resolution is comparable to the upcoming generation of 30 m class telescopes and can serve as a key testing ground for science cases and techniques.

In this Article, we use open-loop Fizeau imaging with the LBTI on an extragalactic target, providing spatial constraints on the structure and heating of the nuclear outflow and dust torus in NGC 1068. These observations reveal low-surface-brightness features at unprobed scales intermediate to single-dish telescopes and long-baseline infrared interferometry.

## Observations and data reduction

On Coordinated Universal Time (UTC) 6 November 2022, we observed NGC 1068, 1 Tau and Procyon using the nulling-optimized mid-infrared camera (NOMIC) instrument[26] on the LBTI in the open-loop Fizeau mode. We used the W08699-9_122 filter ($\lambda_c$ = 8.7 μm, range 8.13–9.35 μm) and took 20 nodding cycles on the target and calibrators, obtaining 59° field rotation. Before and after the science target, we observed 1 Tau and Procyon to serve as flux and point spread function (PSF) calibrators. We later selected images via 'lucky fringing', resulting in an exposure time of 200 × 0.0137 s = 2.74 s per cycle or 54.8 s total exposure on NGC 1068. The resulting corotated and stacked target images and PSF calibrator images are each shown in Fig. 1. See 'Observations and calibration' in Methods for details on frame selection, PSF calibration and flux calibration.

We deconvolved the calibrator PSF from the science target PSF to recover the underlying NGC 1068 source flux distribution. Although this had been done previously for Io[23] with the LMIRCam detector, NGC 1068 is much fainter and extended, and several changes were made to the adaptive optics (AO) system of the LBT[27] in the years following the publication of those data. We therefore performed image deconvolution in three different ways (see 'Image deconvolution' in Methods), finding good agreement between them. We show the results of deconvolution using the Richardson–Lucy method as in ref. 23 in Fig. 2. Other deconvolutions are shown in Extended Data Figs. 1–3. We estimate the resulting resolution using the southernmost and northernmost point sources in the image, measuring full width at half-maximum (FWHM) 47 × 90 mas after deconvolution. In this Article, we focus on the Richardson–Lucy deconvolved images of NGC 1068 because of the robust legacy and fidelity of the method.

## The dusty wind

The circumnuclear region in NGC 1068 has been extensively studied in high resolution at numerous wavelengths. We compare the recovered 8.7 μm morphology at 47 mas (3.3 pc) resolution with existing radio maps (at 5 GHz with 105 × 51 mas resolution[18], optical images ([OIII5007] forbidden line emission with 52 mas resolution[28]) and NIR/MIR observations using single-dish deconvolution (~100 mas resolution[29]) and interferometry[13,30] (74 mas and 3 mas resolution, respectively). We show

https://doi.org/10.1038/s41550-024-02461-y

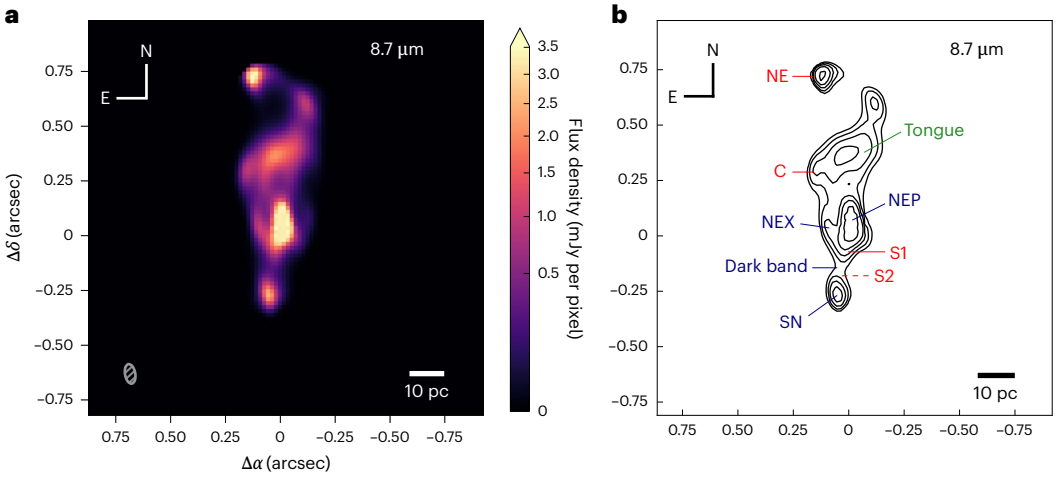


**Fig. 2 | LBTI Fizeau image of NGC 1068 after deconvolution. a**, A Richardson-Lucy deconvolved LBTI Fizeau image of NGC 1068 at 8.7 μm using method 1. **b**, Contours of the same image with feature labels. Contours start at 90% of the peak flux density and decrease by a multiplicative factor of 2 down to a factor 128 below the maximum contour. This image was deconvolved from the stacked-corotated cycles using the Richardson–Lucy method. The resulting resolution FWHM is 46.8 × 90 mas (3.3 × 6.3 pc), shown as an ellipse in **a**. Red and green labels indicate features from the literature (ref. 18 and ref. 29, respectively), and blue labels indicate new features from this work: the NEP, the NEX, the dark band and the SN. The results of other deconvolution approaches are given in Methods.

this comparison in Fig. 3, specifically showing the 5 GHz radio emission, previous single-dish MIR imaging, [OIII] emission and VLTI/MATISSE MIR reconstructed image with respect to our recovered MIR structures.

In the deconvolved images (Fig. 2 and Extended Data Figs. 1–3), we see extended flux along the north–south direction as well as bright point sources to the northeast at 600 mas (45 pc) and to the south at 300 mas (20 pc, called the SN for southern N-band source). The 47 × 90 mas recovered resolution allows us to distinguish substructures near the AGN core. Here, we see extensions of flux from the flux peak towards the north and northeast out to ≥10 pc (150 mas). We refer to this northeast extension hereafter as NEX and the northern extension as NEP. Between the flux peak and the SN there is a drop in emission we refer to as the dark band.

We find morphological agreement with both the radio emission and previous optical-infrared imaging. The authors in ref. 18 locate the SMBH in a structure called S1; similar to positions inferred from maser emission[31], model fitting to MATISSE data[32] and morphological correspondence[13,29], we place the peak of the MIR emission 50 mas north of S1. We then find that the southernmost and northern 8.7 μm structures correspond roughly to peaks in the radio emission (respectively called S2 and C in ref. 18). However, we note in both cases there is an offset of ~50 mas, with the MIR emission found exterior to the radio. The northernmost emission is near the northeast (NE) source of ref. 18, but like in ref. 29 we find a ~100 mas separation between the MIR and 5 GHz emission. The 7.9 μm emission of ref. 29 includes a peak far to the NE that we do not recover. Assuming that the flux of the northeastern component has remained the same since the ref. 29 observations, we would expect a flux density of ~0.68 mJy per pixel, which is above the 2$\sigma$ flux level of the deconvolved image (where $\sigma \cong 0.1$ mJy px$^{-1}$ is the standard deviation of measured pixel values in the image background). Over the same period, the 5 GHz flux of cloud C has been shown to decrease by ~50% (ref. 19); a similar flux change would put this source below our current detection limit. Indeed, when comparing our 144 mas aperture flux of cloud C with the 200 mas aperture flux of ref. 29, we measure approximately one-sixth of the previous value (100 ± 6 mJy at 8.7 μm versus 661 mJy at 7.9 μm).

We see that the northern structures have counterparts in the [OIII] and NIR emission. Notably, our measured NEX feature traces the opening angle of the ionization cone[28]. SINFONI observations of several atomic emission lines ([Fe II], [Si IV], Pa$\alpha$ and HeI) and molecular hydrogen show a similar morphology to the arc of flux starting from C and continuing from the tongue counterclockwise towards NE[20]. The infrared emission is thus coincident with highly ionized, relatively hot gas. The atomic lines are associated with a shock 'bubble' being excavated by the jet[20,33].

Infrared interferometry also shows morphological similarity to the features near the centre of the Fizeau image. In the K′-band bispectrum speckle interferometry images of ref. 30, flux extends from the AGN towards the north ~400 mas. The K′-band emission corresponds in scale and shape to the northern extended N-band flux we image. The authors give a rough flux range of 30–230 mJy; in our northern aperture, we measure ~100 mJy. The K′-band flux range is too large to reasonably estimate a dust temperature at this location. The VLTI/MATISSE observations[13] and modelling[32] indicate the continuation of NEX down to subparsec scales. In the modelling work[32], this is the southern edge of a dusty (outflow) cone. In the model-independent imaging[13], the N-band emission also shows an X shape similar to the Atacama Large Millimetre Array (ALMA) emission[16] and the edges of the [OIII] emission. The match in position angle (PA) of the LBTI Fizeau NEX, the VLTI/MATISSE 'X' and the ALMA 256 GHz map[16] strongly indicates that this is the same structure measured at different scales.

Using apertures with a diameter of 10.1 pc, we measure the flux at two image locations: the flux of the southern component (SN) is $F_{\mathrm{South}} = 39.6 \pm 2.4$ mJy, with the aperture centred 25.1 pc to the south of the centre; at the same distance to the north we measure $F_{\mathrm{North}} = 100.6 \pm 6.2$ mJy. Using equation 1 from ref. 34 and the relation $F(r) = \sigma A T(r)^4$, we calculate an expected dust flux in an aperture with area $A$ as a function of radius ('(Non)thermal dust emission along the radio jet' in Methods). The observed values are far above the simple prediction, as is readily seen in Fig. 4. At distances of 20 pc and 45 pc, the flux excesses are associated with 5 GHz features C and NE. Spectral index measurements of cloud C show steep spectra indicative of optically thin, non-thermal emission between 5 GHz and 21 GHz (ref. 19). We use the spectral index and 5 GHz integrated flux of C to estimate a jet flux at 8.7 μm of 0.06 mJy. The non-thermal contribution is thus quite small. It is therefore likely that a mixture of non-thermal emission and shock heating is necessary to produce the MIR fluxes. The exact contributions from non-thermal radiation and shock-heated dust are beyond the scope of this work. The correspondence between the different observations indicates that the MIR emission simultaneously

https://doi.org/10.1038/s41550-024-02461-y

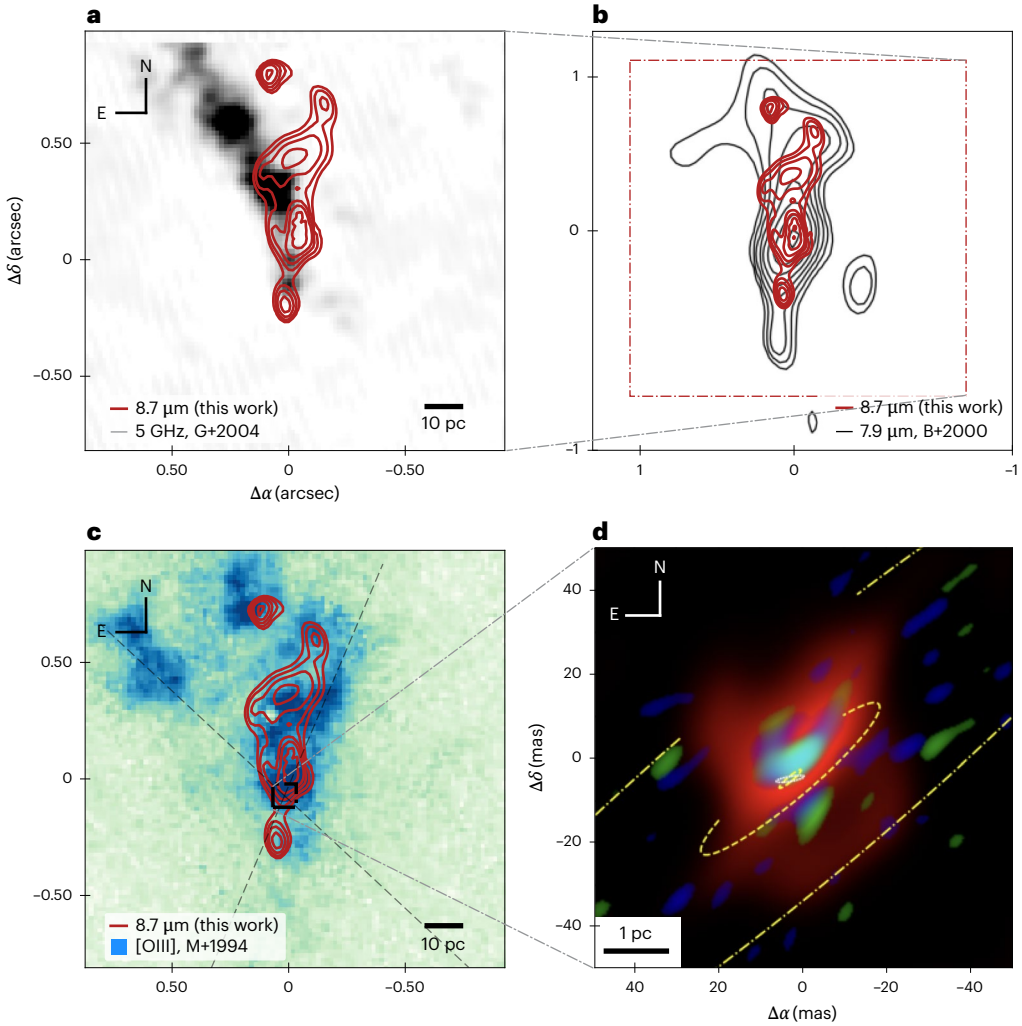


**Fig. 3 | Comparison of deconvolved LBTI Fizeau image to observations at other wavelengths. a**–**c**, Deconvolved LBTI Fizeau image of NGC 1068 at 8.7 μm compared with observations of the 5 GHz radio emission (**a**, ref. 18), the single-dish 7.9 μm emission (**b**, ref. 29) and the ionization cone traced by [OIII] (**c**, ref. 28). **d**, The MIR emission at subparsec scales as observed with VLTI/MATISSE (L band in blue, M band in green and N band in red). The spur to the northeast of centre found in the LBTI image is seen at the subparsec scale in the VLTI/MATISSE image. The yellow ellipses represent the orientation of the obscuring dust disk. The red contours are the same as in Fig. 2. Panel **d** reproduced with permission from ref. 13, Springer Nature Limited.

traces AGN-heated dust, jet–cloud interactions in C (and possibly S2), and highly ionized jet shocks in the tongue. Our observations lack precise astrometry, but independent morphological similarity to the radio, MIR and [OIII] observations constrains our positions to within a few pixels (≤3 pixels = 54 mas, or one PSF width).

## Constraints on the dusty torus

The disk+wind model consists of a geometrically thin, optically thick equatorial disk and a conical structure perpendicular to it (usually with hyperbolic or parabolic walls) representing a radiation-driven wind. This morphology was recently shown to be a good representation of the VLTI/GRAVITY and VLTI/MATISSE data for NGC 1068 (ref. 32), but the interferometric data resolved out structures larger than ~5 pc. We computed a disk+wind radiative transfer (RT) model out to 15 pc using the SKIRT (Stellar Kinematics Including Radiative Transfer) code[35]. The parameters of the RT modelling are given in 'Radiation transfer modeling' in Methods. The model was based on the one presented in ref. 11 with clumpy graphite dust in a hyperboloid cone and graphite–silicate dust in the disk. Surface brightness profiles of the resulting simulated and observed flux distributions are shown in Fig. 4.

Many observed features on <15 pc scales (for example, NEX, the dark band and SN) and the north–south asymmetry of the large-scale emission are reproduced by the disk+wind model (shown in Extended Data Fig. 4): near the central flux peak we see an edge-brightened outflow cone like NEX; south of the flux peak is a dark absorption band due to the densest part of the disk; and the ~75°-inclined disk out to ≥25 pc causes extinction towards the south. The observed morphology, however, is not purely a disk+wind. There is much more flux directly north of the AGN in the images than in the modelling—this follows the path of the radio jet and is probably emission from jet–cloud interactions. Based on deviations from a centrally heated flux profile, correspondence with radio jet and shock morphology, and 5–21 GHz spectral indices of the sources, we claim that a large fraction of the MIR emission we recover is actually related to the radio jet (either directly or through, for example, shock heating) rather than the radiation-pressure-driven wind. Through comparisons with RT models as well as to multiwavelength observations, we are able to spatially distinguish two separate AGN–host interaction channels at 3.4 pc resolution, showing a disk+wind(+jet) morphology. Previous VLT imaging[36] supported the disk+wind model but did not have sufficient resolution to distinguish jet-related features.

The dusty wind, ionization cone and radio jet are all presumed to be symmetric above and below the accretion disk. Based on correspondence with the radio data, we place the SMBH at the location

https://doi.org/10.1038/s41550-024-02461-y

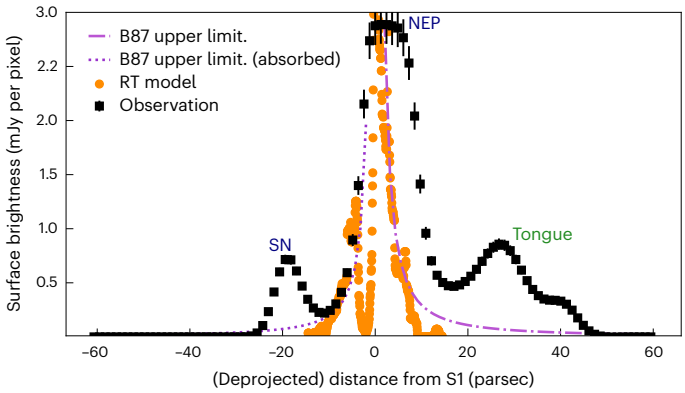


**Fig. 4 | Surface brightness profiles of the observations and RT modelling.** Distances have been deprojected using an inclination of 75° from face on. The error bars on the observed surface brightness come from uncertainty in flux calibration, typically ≲10%. We estimate an upper limit to the thermal dust flux as a function of radius. The dashed line shows the predicted upper limits, and the dotted line shows the upper limits obscured by $\tau_{8.7} = 0.41$. We also plot the measured flux values from a disk + wind radiation transfer model out to 15 pc. Corresponding features from Fig. 2 are labelled.

marked with a green X in Fig. 5, near the bottom of the brightest flux region. If we then assume that similar structure should extend to the north and south, it is immediately apparent that some absorbing medium is present—probably the disk-like component of the dusty torus. We estimate the optical depth of this dusty structure by relating the flux at an equal distance (accounting for inclination) above and below the SMBH ('Optical depth' in Methods). Using the same apertures as above, we find that the southern emitting region is being obscured by an object with an optical depth of $\tau_{8.7} = 0.41 \pm 0.04$. This obscuring structure is assumed to be the disk-like component of the disk+wind model (for example, refs. 32,37). The optical depth of such a structure is expected to increase approaching the SMBH. We have measured the average value at 25.1 pc within a 10.1-pc-diameter aperture. Assuming a linear change in $\tau$, we obtain an optical depth gradient of $-0.05\ \mathrm{pc}^{-1} \leq \Delta\tau_{8.7\mu m} \leq -0.02\ \mathrm{pc}^{-1}$ when comparing with VLTI/MATISSE <1 pc scale measurements[13].

The dark band between the flux peak in our images and the southernmost emission is inferred to be due to an obscuring dust disk centred on S1. VLTI/MATISSE observations revealed a similarly oriented obscuring dust disk[13,32] (plotted as yellow ellipses in Fig. 3d, reproduced from ref. 13). A molecular torus observed with CO(2–1), CO(3–2) and $HCO^+$(4–3) (ref. 17) is oriented approximately perpendicular to the radio jet, similar to the orientation of the obscuring dark band we and VLTI/MATISSE observe. We estimate that the 75°-inclined obscuring disk has a diameter ≥70 pc to obscure SN. This is more than twice as large as the 30 pc CO disk measured by ALMA[17]; the discrepancy may indicate that CO traces the densest, inner parts of the disk, but a more extended region still contributes to obscuration.

Finally, using the assumed geometry and inclination of the circumnuclear structures, we estimate a lower limit on the dust density within the obscuring dark band to be $\rho_{dust} \geq 9 \times 10^{-27}\ \mathrm{g\ cm^{-3}}$. Compared with average interstellar medium (ISM) gas density, this corresponds to 60% of the standard ISM dust–gas ratio of ~1% (ref. 38). A study of 36 X-ray-observed AGNs yielded dust-to-gas ratios in the range 1–100% the standard ISM value[39]. Our measurement falls within this range, but we note that the local density can be much higher if the dust is located within a thin disk as models predict. Future RT modelling is necessary to test the implications of the optical depth gradient on the disk's density profile.

The methods used herein can be applied to other AGN to understand the applicability of the disk+wind(+jet) as a unified model of AGN. Based on the measured fringe signal-to-noise ratio (SNR) of these observations, 324.26 ± 76.17 for the 20 cycles of NGC 1068 (10.2 ± 3.6 Jy) and 307.22 ± 28.17 for the 7 good cycles of 1 Tau (11.2 Jy), we estimate that we could achieve SNR ≥10 for sources ≥0.3 Jy with roughly 1 min total integration. This is certainly optimistic due to decreased AO performance on faint sources, but repeated observations, more cycles or fringe tracking on a nearby star could overcome this. We cross-matched the AGN catalogue of ref. 40 with the All Wide-field Infrared Survey Explorer (ALLWISE) catalogue[41] to search for sources. Given the 0.3 Jy N-band flux cut-off, we use *W*3 as a proxy to identify 24 sources that are bright enough in N and have $V < 15$ for AO tracking. This sample of northern AGN includes roughly equal numbers of Seyfert 1 and Seyfert 2 systems and would allow a population study comparable in scope to the VLTI/MIDI sample[9,10] that caused the paradigm shift to disk+wind models.

## Conclusions

In this Article, we present extragalactic results from open-loop Fizeau imaging with LBTI/NOMIC. We observed NGC 1068 with a 22.8 × 8.4 m synthetic aperture at 8.7 μm; after PSF deconvolution, we obtained a measured 47 × 90 mas (3.3 × 6.2 pc) resolution. Through the resulting images, we resolved substructures of the circumnuclear dust, tested the current paradigm of disk+wind AGN models and spatially distinguished the dusty wind from jet–host interactions. More specifically, in this work we:

(1) developed the methods to deconvolve the PSF of complex, large-scale emission in LBTI/NOMIC Fizeau images;
(2) used the correspondence between the Fizeau images and existing observations of the 5 GHz, [OIII], NIR lines, and MIR dust emission to identify different emission mechanisms and to create a self-consistent schematic of the MIR dust emission from subparsec to ~100 pc scales;
(3) identified the NEX—a morphological feature that extends NE from the subparsec-scale MATISSE structure and traces the southern edge of the ionization cone—which we claim is the resolved onset of AGN feedback via dusty winds and in agreement with the current disk+wind unified model paradigm;
(4) measured the radial flux distribution of the 8.7 μm emission, identifying clear excesses beyond the radiative dust heating of the classical AGN torus model (by the accretion disk) at 20 and 45 pc from the AGN, and postulating that this excess emission is due to dust–jet interactions and shocks based on correspondence with the 5 GHz emission and NIR emission lines;
(5) measured the optical depth of the inferred obscuring disk of the disk+wind model to be $\tau_{8.7\mu m} = 0.41 \pm 0.04$ between 20 and 30 pc radial distance from the AGN. From this, we infer a lower limit on the dust density of the obscuring material to be $\rho_{dust} \geq 9 \times 10^{-27}\ \mathrm{g\ cm^{-3}}$.

These results show the interplay between jet-mode and quasar-mode feedback, as we find signatures of dust–jet interaction and dusty, radiation-pressure driven winds in the ionization cone. The disentanglement of jet emission, shocks and dusty winds is important for the interpretation of observations with telescopes such as JWST in which the processes are blended due to lower resolution. We additionally constrain the obscuring disk in the disk+wind flavour of the unified model of AGN. Future observations with this mode utilizing the L-band and/or other narrow N-band filters will allow us to measure spatially resolved dust temperatures and further constrain emission processes. Finally, we have presented Extremely Large Telescope (ELT)-scale images of an extragalactic source, developing the methods and tools necessary to make this LBTI observing mode usable for general science cases and tests for upcoming facilities.

https://doi.org/10.1038/s41550-024-02461-y

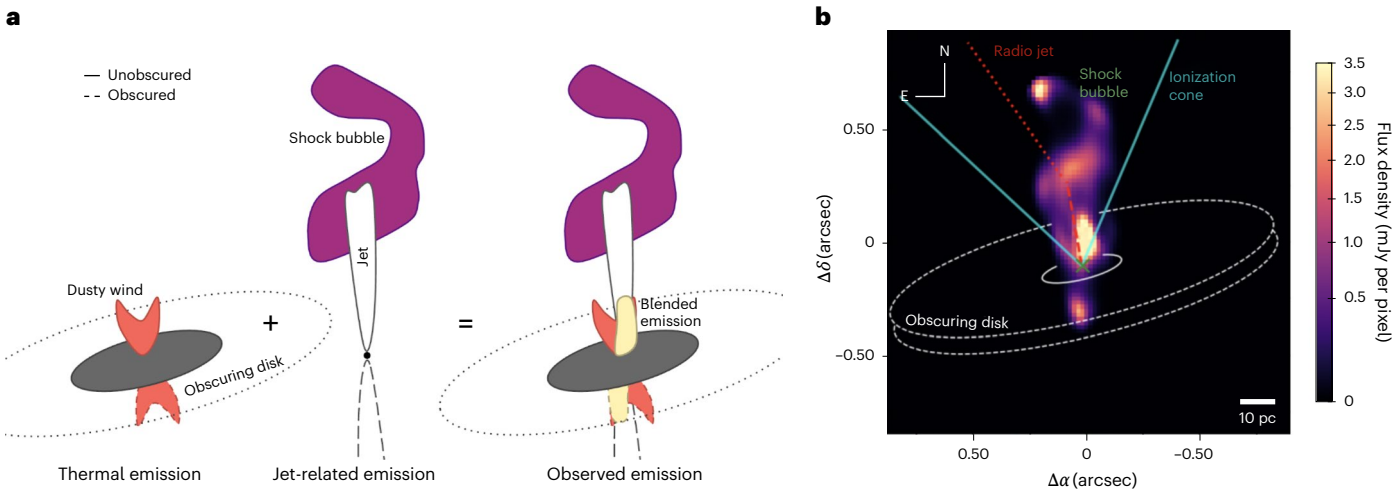


**Fig. 5 | Schematic summary of the subparsec to ≳100 pc scale processes measured with the MIR emission. a**, A cartoon decomposition of the emission processes we identify. **b**, The image from Fig. 1 with labels identifying features observed in different wavelengths. The direction of the radio jet (including the bend at cloud C) is shown in red. The edges of the ionization cone are shown in cyan. The location of the SMBH is marked with a green X on the basis of the S1 position in ref. 18. Finally, an obscuring dust disk is indicated with white ellipses; this disk extends far enough to cover the assumed southern emission features with an optical depth of $\tau_{8.7\mu m} = 0.41 \pm 0.04$.

# Methods

## Observations and calibration

On 6 November 2023, we observed NGC 1068, 1 Tau and Procyon using the NOMIC instrument on the LBTI in the open-loop Fizeau mode. We used the W08699-9_122 filter ($\lambda_c$ = 8.7 µm, range 8.13–9.35 µm) and took a number of nodding cycles on the target and calibrators consisting of 4,000 exposures of 0.014 s (2,000 exposures on target, 2,000 exposures on sky). Between 05:34:42 UTC and 08:48:58, 20 nodding cycles towards NGC 1068 were observed. Before and after the science target, we observed 1 Tau and Procyon to serve as flux and PSF calibrators.

To identify good and bad chop–nod cycles, we inspect the peak flux of each cycle throughout the night. Bad cycles are expected to be those with large thermal background variations or thin clouds. We plot the peak flux over time of both NGC 1068 and 1 Tau in Supplementary Fig. 1. From this we see that 1 Tau produced the same peak flux values at the beginning and end of the night, indicating a stable thermal background. We can, however, identify two cycles with low peak fluxes. Upon inspection, we find that these were affected by thin cirrus clouds causing a variable background and bad adaptive optics performance. We discard these when computing statistics for the 1 Tau PSF. For both 1 Tau and NGC 1068, the cycle-to-cycle flux variations are found to be similar to the peak flux variations within a cycle. We conclude that neither the mean PSF nor the flux calibration changes throughout the night. This allows us to work with stacked images.

The ideal PSF of the LBTI is the interference pattern of two 8.4 m circular apertures separated by 14 m. The resulting 22.8 m maximum baseline gives 78.7 mas resolution (5.5 pc) at 8.7 µm. The interference fringes exhibit a narrow central fringe peak, and a set of side lobes that rapidly decrease in amplitude as one moves further from the centre. We refer to the interference fringe pattern as a Fizeau PSF. Over the span of approximately 3 h on target, there was 59° field rotation. Field rotation causes the 22.8 m baseline of the LBTI to probe the target at different angles; after 180° field rotation this approximates a single 22.8 m telescope. Simulated field rotation on a real Fizeau PSF exhibits an approximately circular, 22.8 m PSF after ~60° (ref. 42). Robust estimates of both the individual cycle PSF and the PSF after field rotation are necessary for proper image deconvolution to recover the true flux distribution of the science target. The resulting corotated and stacked target and PSF calibrator are each shown in Fig. 1.

Fringe tracking was done in the so-called open-loop mode, which means that not all frames are necessarily at the zero-order (or white-light) fringe and may jump due to atmospheric shifts to higher-order fringes that are not useful for this study. However, the source was also imaged on the LMIRCam[43] detector in the L band (2.8–4.1 µm) and the Fizeau PSF was spectrally dispersed. The interferometric phase on LMIRCam (which in Fizeau imaging has the same optical path delay as NOMIC) was set to the white-light fringe, and phase shifts were corrected manually by keeping the fringes straight. While the NOMIC fringes moved due to atmospheric piston during and between exposures, this ensured that the movement was generally centred around the white-light fringe.

The Fizeau PSF may also move in the image plane or the two individual telescope PSFs may become slightly misaligned due to residual jitter from the AO system, although this effect is generally small compared with the 8.4 m N-band PSF and the precision at which the two PSFs can be overlapped (~10 mas differential tip–tilt jitter[22,44]). We account for both of these effects using lucky Fizeau fringing, that is, we discard exposures with misaligned fringes or poorly overlapped telescope beams. We first compute the two-dimensional (2D) cross-correlation function between the theoretical PSF and each frame of our observed PSF calibration stars. In each nodding cycle, we keep the frames that have the 10% largest cross-correlation values—in other words, the 10% of frames most similar to the theoretical PSF (a similar approach was used in ref. 45). The selection of 10% is somewhat arbitrary, but larger values tend to decrease the peak SNR of the PSF image by blurring the PSF, and smaller values have too few frames to build up a robust empirical PSF estimate. Within each nodding cycle, the top 10% of frames are stacked, with each frame having been shifted to the pixel location with the highest 2D cross-correlation value, typically ≤3 pixels (pixel scale is 17.9 mas per pixel).

Two cycles of 1 Tau (cycles 5 and 6) showed large deviations from the theoretical PSF, with broad, blurred artefacts. Upon closer inspection, these cycles suffered from light cirrus passing through. We therefore discard them as outliers. The remaining target and calibrator stacked PSFs show stability throughout the night. Finally, we compute the mean PSF for each calibration star. The mean PSF for 1 Tau is used in the following as our empirical PSF estimate because its flux (11.3 Jy (ref. 46)) is more similar than Procyon's (74 Jy (ref. 46)) to that of NGC 1068 (10.2 ± 3.6 Jy (ref. 47)), and so noise estimates are similar.

The empirical PSF is shown in Fig. 1, illustrating the characteristic triple-peak fringe pattern of the LBTI.

Good frames of NGC 1068 were selected in a similar way as for the PSF calibrators. Within each nodding cycle, we compute the 2D cross-correlation function between NGC 1068 and a nominal PSF (in this case, the measured PSF from the calibrator star). The frames with the 90th-percentile largest cross-correlation values are kept. As before, the target frames are recentred to the pixel location with the peak 2D cross-correlation value and then stacked.

We obtain 20 stacked images of NGC 1068, one for each nodding cycle throughout the night. The resulting stacked image from each nodding cycle is shown in the Methods. Ten per cent of frames corresponds to 200 frames per cycle; this results in exposure time of 200 × 0.0137 s = 2.74 s per cycle or 54.8 s total exposure on NGC 1068. Before stacking each cycle, we corotated each subframe such that north is oriented along the *y* axis in the frame. To create an estimate of the final, rotated PSF, we corotated the PSF calibrator frames by the same amount as the target subframes within each cycle and stacked.

We use the MIR stellar diameters and fluxes compilation catalogue (MDC[46]) to obtain the N-band fluxes of the calibrators. As is typical, we assume that the unresolved stellar flux is distributed completely within the Fizeau PSF of the calibrator. This gives us a scaling between counts and jansky in each pixel that we apply to the science target. The results are consistent between Procyon (74 Jy) and 1 Tau (11.3 Jy), but we use the values from 1 Tau because it is closer to the nuclear flux of NGC 1068 (10.2 ± 3.6 Jy (ref. 47)) and, thus, has a similar SNR.

As LBTI Fizeau imaging is rather new to the community, we summarize the main differences from traditional, single-aperture observations. First, the Fizeau PSF is characterized by a triple-peaked fringe pattern, yielding 22.8 m resolution in one direction and 8.4 m resolution in the orthogonal direction. We show that even small amounts of field rotation allow one to obtain resolution better than 8.4 m in all directions, although a circular PSF would require 180° rotation[42]. Second, for non-ideal field rotation (and generally for the non-circular PSF of any segmented primary mirror), the effects of the resulting elongated PSF can be removed using image deconvolution. While image deconvolution is rather commonplace for observations with for example, Keck[29] or JWST[48], we explore various methods below for the specific LBTI configuration. Third, we used lucky fringing, keeping only the best 10% of data. This extremely conservative approach was feasible due to the brightness of the source, but recently published LBTI results have shown that ≥90% of frames can be kept in some cases for Fizeau imaging[42], greatly increasing observation efficiency. For sources with *K*-band magnitude < 4.5 mag, fringe-tracked imaging can be performed, removing the need for frame selection. A scheduled upgrade to the fringe tracking detector will increase this limit to $K < 10$ mag (ref. 49). Finally, because the Fizeau aperture consists of two 8.4 m telescopes, the collecting area equivalent to that of an 11.9 m telescope (111 $m^2$). Upcoming facilities, such as the ELT and the Giant Magellan Telescope (GMT), will have larger effective collecting areas (978 $m^2$ and 368 $m^2$, respectively) and, thus, higher sensitivity than the LBTI.

## Image deconvolution

As can be clearly seen in Fig. 1, the stacked and corotated science cycles exhibit obvious artefacts due to the Fizeau PSF. Whereas extended flux features are still discernible, small-scale features near the centre of the image are dominated by these artefacts. Using empirical measurements of the Fizeau PSF in individual cycles and for the stacked image, we can deconvolve the known PSF features to reveal the underlying source flux. This was previously done in ref. 23 for observations of Io, but in the intervening years there have been changes to the adaptive optics performance of the LBTI[27] and we used the NOMIC detector instead of LMIRCam. We therefore attempt Fizeau PSF deconvolution in three different ways: the first two use Richardson–Lucy deconvolution as in ref. 23, and the third was developed for this work on the basis of the Högbom CLEAN algorithm[50].

**Richardson–Lucy deconvolution.** We proceed two different ways using Richardson–Lucy deconvolution[51,52]:

(1) stack all corotated frames and deconvolve with a stacked, corotated PSF estimate or
(2) deconvolve the image from each cycle with the PSF calibrator and then stack the resulting images.

The first method has the benefit of doing as few convolutions as possible (each introduces noise) at the expense of requiring that the estimate of the final PSF is robust. The second method uses a robust, single-cycle PSF but requires 20 (lower SNR) deconvolutions instead of one. In both cases, we use Richardson–Lucy deconvolution (from scikit-image.restore) because of its robustness to noise and efficiency. We find that both sequences give similar results, which is a strong indication of the validity and robustness of the target flux distribution we recover. In practice, stacking before deconvolution (method 1) increased the SNR of faint features, as noise is added destructively. This led to more stable results when changing the parameters n_iter and filter_epsilon (the number of iterations and the clipping value for avoiding division by zero, respectively).

We estimate the uncertainty of each pixel in the resulting images using a bootstrap method; we perturbed the empirical PSF by Gaussian noise and reperformed the deconvolution numerous times. For the images presented in Figs. 2, 3, and 5 we used method 1 with n_iter = 32 and filter_epsilon = 0.005; we show the results in Fig. 2. The total flux of the image was not conserved during deconvolution, and therefore the deconvolved image is renormalized so that the total flux of the resulting image equals the total flux of the corotated + stacked image (specifically, it is scaled by a factor of 0.7). The resulting PSF is 46.8 × 90 mas FWHM.

As expected from previous observations, we see extended flux along the north–south direction as well as a bright point source to the northeast at 600 mas (45 pc). However, the 78 mas PSF from the 22.8 m baseline allows us to resolve the inner substructure near the AGN core. Here, we see a spur of flux pointing towards the northeast out to ~10 pc. In the deconvolved-then-stacked (method 2) image, we see evidence of an additional, smaller spur to the northwest. These spurs are found near the expected AGN location and are oriented in a similar direction as extended N-band dust measured on smaller scales with MATISSE[13]. In method 2, we find that the bad channel (visible in Supplementary Fig. 2 in the upper third of the images) causes more artefacts than in method 1. In Extended Data Fig. 1, we see a negative contour at the location of the bad channel when using method 2. It seems that the stacking of images in method 1 washes out the effects of this channel. Due to the stability of the PSF throughout the night that allows robust image stacking and the strong artefacts present in method 2, we use method 1 for analysis throughout this Article. We note, however, that the results change by only a few per cent when using the other deconvolution method.

**CLEAN-inspired method.** The Högbom CLEAN algorithm is an aperture synthesis algorithm, developed to deconvolve a known beam from a measured radio emission map affected by prominent and extended sidelobes[50]. Similarly, the known ideal Fizeau PSF produced by the LBTI has prominent and extended sidelobes. Due to the high fidelity of CLEANed radio images, we developed an experimental implementation for LBTI Fizeau images that iteratively removes the known, extended PSF.

We use the following notation: $Im_0$ is the initial, dirty image to deconvolve, beam is the known PSF estimate, gain is scaling applied to the PSF to remove flux from the dirty image in each iteration, CUTOFF is the flux level to which the image is cleaned, MAXITER is the maximum

number of iterations to compute and peak is the maximum flux in the current image, $I_i$. The algorithm then proceeds as follows:

START
WHILE peak > CUTOFF AND $n_{iter}$ < MAXITER

(1) Find peak flux in image, at coordinates $(x_p, y_p)$
(2) Create $Im_{i+1}$
- Create a zero-image with same dimensions as $Im_0$
- Place a point source with flux = gain × peak at $(x_p, y_p)$ and convolve with beam
- Subtract this from $Im_i$ to get $Im_{i+1}$

(3) Put a point source at $(x_p, y_p)$ in the CLEAN image
(4) $n_{iter} = n_{iter} + 1$

ENDWHILE
END

We applied the above method with gain of $10^{-4}$ and MAXITER of $10^6$ on each of the 20 exposure cycles. We also set CUTOFF as mean($Im_0$), that is, stop when the iteration peak is just above the background level. We finally corotate and stack the images as above. The resulting, deconvolved image is shown in Extended Data Fig. 2. The results of this method show more low-surface brightness features than the Richardson–Lucy deconvolution in Fig. 2; in particular, the flux extending to the south of the photocentre and the flux within the northernmost arc are more prominent in the CLEAN-inspired deconvolution. Importantly, the spur extending to the NE of the photocentre appears in this deconvolution as well, with a similar opening angle and length. The fact that this feature appears in this independent deconvolution method gives yet more credence to its fidelity.

**Neural network deconvolution.** The method presented here is a new algorithm developed to perform image deconvolution without using an experimental PSF. Instead, we use a neural network trained on a large dataset of simulated LBTI observations. This method is derived from the interferometric image reconstruction algorithm proposed in ref. 53. The results are shown in Extended Data Fig. 3.

The algorithm steps are as follows:

(1) Generate a large set of mock astrophysical images.
(2) Simulate random LBTI PSFs, convolve the images with these PSFs and introduce noise.
(3) Train a neural network to restore the original images using only the simulated data.
(4) Apply the trained neural network to the actual astronomical observation.

We elaborate on these steps in the subsequent paragraphs.

*Generation of mock astrophysical images*. The objective is to rapidly produce a diverse set of images containing varied structures with different spatial scales. We create each image by summing several component images, each representing structures at a characteristic spatial scale, $\lambda$, randomly selected between one pixel and the full field of view. The number of component images, $N$, varies randomly from 1 to 20. For each component, we:

(1) Compute a 2D discrete exponential power spectrum $P$ with characteristic scale $\lambda$.
(2) Assign a random phase $\phi$ to each pixel.
(3) Calculate the real part of the Fourier transform of $P \times e^{i\times\phi}$ and mask the negative values.

The $N$ images are combined using random weights, and the total flux of the resultant image is normalized to unity. This process is repeated to generate $2^{20}$ unique images of dimensions $(n_{pix} \times n_{pix})$, with $n_{pix} = 100$.

*Simulation of observations*. Each generated image is then used to simulate an observation cube with dimension $(n_{frames}, n_{pix}, n_{pix})$, with $n_{frames} = 32$. The decision to use data cubes with $n_{frames}$ rather than a single frame is driven by two factors: first, this approach allows the neural network to prioritize data from the highest-quality frames, thereby optimizing image selection; second, it enables the differentiation of PSF variations—which change from frame to frame—from static astrophysical elements.

Instantaneous PSFs are computed as the Fourier transform of $Pup \times \exp(i \times \phi_{res})$, where Pup is the telescope pupil and $\phi_{res}$ is the residual atmospheric phase postadaptive optics correction. The pupil is modelled as two 8.4 m disks, each with a central 0.9 m obstruction, and a 14.4 m centre-to-centre separation. $\phi_{res}$ is calculated from a sum of Zernike polynomials with coefficients randomly selected following a power-law distribution $P(n) \propto n^{-\alpha}$, where $n$ is the radial order of the polynomial.

A number $n_\tau$ of these instantaneous PSFs, drawn uniformly between 1 and 100, are averaged to create a semi-long exposure PSF. Each image is then convolved with $n_{frames}$ such PSFs, creating an observation data cube.

Two types of normal noise are added to the datacube, one proportional to the square root of the surface brightness of the images (photon noise of the source) and one uniform across the field of view (photon noise of the subtracted sky). The overall noise level is randomly drawn for each observation to produce a SNR between 1 and 50 for individual frames.

*Neural network and training*. After generating the training dataset, consisting of $2^{20}$ random images and the corresponding observations, we train a neural network to reconstruct the original images from these convolved, simulated datasets.

We use a simplified version of the U-Net architecture, which is fully convolutional and includes skip layers. A schematic is shown in Supplementary Fig. 4.

The training is done on 50 epochs, each one including the entire dataset in batches of 16 observations. We use the Adam optimizer with a mean absolute loss function and an initial learning rate of $5 \times 10^{-4}$. This learning rate is halved each time there is no improvement in the loss after five consecutive epochs. The final mean absolute error, indicating the difference between the network's prediction and the actual original images, is 0.09 for both the validation and the training dataset, demonstrating that the training did not result in overfitting.

*IV. Application to the actual observations*. The observations consist of 20 cycles, corresponding to 20 different orientations of the source in the plane of the sky, each of these cycles corresponding to 2,000 individual short-exposure frames.

We split each of these 2,000 frame sets into 62 data cubes each with 32 frames, which were fed to the trained neural network, hence producing 62 deconvolved images for each orientation. These 62 deconvolutions are then averaged to produce one image per orientation. The 20 resulting images are then derotated, and the final image is computed as the median of these images (Extended Data Fig. 3). The low-surface-brightness features are better recovered than in Fig. 2 and resemble those of the CLEAN approach in Extended Data Fig. 2. The central emission is more compact than the CLEAN deconvolution results but shows a similar northwest–southeast extension. The NEX feature, however, is not as readily apparent in these results, athough the flux envelope near the centre traces roughly the opening angle of the ionization cone.

**Estimating image significance.** The standard deviation of the cycle PSFs is used as an uncertainty estimate, allowing us to bootstrap errors of the deconvolution we perform on the target frames. In Supplementary Fig. 5, we show the PSF images and flux profiles of all 1 Tau cycles.

We compute the per-pixel mean and standard deviation of all cycles (excluding cycles 5 and 6 owing to thin cirrus). In 1,000 bootstrap iterations, we perturb the empirical PSF (Fig. 1) with random noise set by the standard deviation at each pixel. We then stack and corotate the perturbed PSF to match the rotations of the 20 target observing cycles. From the 1,000 iterations, we can compute the uncertainty per pixel for the recovered deconvolved images below; from this we conclude that all primary structures in the image (the central component with a spur, the southern point source, the northern extended structure and the northernmost point source) are robustly recovered at $\gtrsim 10\sigma_{\mathrm{bootstrap,px}}$. As an example, we display the SNR map for deconvolution method 1 with 8.7 μm image contours overlaid in Supplementary Fig. 6; this shows that all primary features of the image are found at SNR >10.

### (Non)thermal dust emission along the radio jet

With apertures having a diameter of 8 pixels (0.144 arcsec, 10.1 pc), we measure the flux at several image locations. We measure the flux of the SN to be $F_{\mathrm{South}} = 39.6 \pm 2.4$ mJy, with the aperture centred 25.1 pc to the south of the centre. At the same distance to the north (in cloud C), we measure the flux to be $F_{\mathrm{North}} = 100.6 \pm 6.2$ mJy.

Utilizing equation 1 from ref. 34, we can estimate dust temperature as a function of radius

$$T_{\mathrm{gr}}(r) = 1{,}650\left(\frac{L_{\mathrm{acc}}}{r^2}\frac{\mathrm{pc}^2}{10^{10}\,\mathrm{L}_\odot}\right)^{1/5.6} \mathrm{e}^{-\tau_{\mathrm{uv}}/5.6}\mathrm{K}, \quad (1)$$

where $L_{\mathrm{acc}}$ is the luminosity of the accretion disk in $\mathrm{L}_\odot$, $r$ is the distance from the accretion disk in parsec and $\tau_{\mathrm{uv}}$ is the optical depth to the ultraviolet continuum. The luminosity of grains of this temperature is then $L_{\nu,\Omega}(r) = \sigma/\nu\pi \times T_{\mathrm{gr}}(r)^4\ \mathrm{W\,m^{-2}\,Hz^{-1}\,sr^{-1}}$. The predicted thermal dust flux in an aperture is $F_{8.7\mu\mathrm{m,therm}} = L_{\nu,\Omega}(r)A$, where $A$ is the aperture area. We show in Fig. 4 that there are statistically significant flux excesses 20 and 45 pc from the core that are associated with 5 GHz features S2, C and NE.

The contribution from non-thermal sources within cloud C is very small in the MIR. The authors in ref. 54 present several possible dust-heating mechanisms within shocks for NGC 1068, but there has been some disagreement in the literature about the prevalence of shocks along the radio jet in NGC 1068. The authors of ref. 55 claim that shocks are necessary to heat the dense clouds at their position 2 (cloud C in ref. 18), but the authors of ref. 56 claim that photoionization could be sufficient with different assumptions of cloud densities. More recently, ref. 57 showed high cloud column densities, indicating that shocks are indeed required.

The MIR emission of NGC 1068 in the central 50 pc seemingly requires contributions from several distinct thermal and non-thermal processes. Future LBTI observations of this and other AGN, either with a number of L-, M- or N-band filters to obtain dust colour temperatures or with narrow filters targeting emission lines (for example, [S IV] 10.5 μm and [Ne II] 12.8 μm), will be able to distinguish the emission or heating mechanisms.

### Radiation transfer modelling

The models that most closely match interferometric data of nearby Seyferts (for example, refs. 32,37) consist of a compact, dusty disk and a hollow hyperbolic cone extending in the polar direction. Here, we modify the best-fitting disk+wind model of ref. 37 to use the luminosity of NGC 1068 ($10^{12}\ \mathrm{L}_\odot$) and the opening angle and inclination fit by ref. 32. We then increase the box size of the preexisting small-scale circumnuclear model to measure the flux at 15 pc scale. Except when otherwise listed, the parameters of the disk+wind model are the same as used in ref. 11. We use $i = 75°$, a hyperbolic cone opening angle $\theta_{\mathrm{open}} = 45°$, an outer extent of the hyperbolic cone of $r_{\mathrm{hyp,out}} = 24$ pc, a disk optical depth of $\tau_{\mathrm{disk,9.7}} = 15$ (the same as in ref. 11) and a disk outer radial extent of $r_{\mathrm{disk,out}} = 10$ pc. We also set the instrument field of view to 30 pc and the number of pixels in each direction to 600 pixels. The resulting model is shown in Extended Data Fig. 4, and we also extract radial flux profiles to compare with our measured emission profiles.

The main goal of the RT modelling was to determine whether the NEX in our images could realistically be centrally heated dust in a windy outflow. Morphologically, there is indeed a similar structure due to edge brightening of the wind. To test whether the flux was plausible, we placed an aperture (3.8 pc radius) at approximately the same location in both the Fizeau image and the RT model. The aperture was placed on the southern edge of the ionization cone in both cases, 7 pc from the nucleus. The RT model aperture contains ~100 mJy of flux with a peak flux density of 1.2 mJy per pixel. The observation aperture contains 49 ± 3 mJy with a peak flux density of 1.5 mJy per pixel. While a detailed comparison of the resulting fluxes is not meaningful, the disk+wind RT model shows that it is plausible that the emission in the NEX is AGN-heated dust at the edge of the outflow cone. A detailed RT model parameter study, comparing with the combined VLTI/GRAVITY, VLTI/MATISSE and LBTI data, will be the subject of future work.

### Optical depth

The dusty wind, ionization cone and radio jet are all presumed to be symmetric above and below the accretion disk. Based on correspondence with the radio data, we place the SMBH at the location marked with a green X in Fig. 5, near the bottom of the brightest flux region. If we then assume that similar structure should extend to the north and south, it is immediately apparent that some absorbing medium is present—probably the disk-like component of the dusty torus.

The optical depth is given by

$$\tau = -\ln\frac{F_{\mathrm{South}}}{F_{\mathrm{North}}} = lN\sigma = l\kappa\rho, \quad (2)$$

where $F_{\mathrm{South}}$ and $F_{\mathrm{North}}$ are the fluxes equidistant south and north of the SMBH, $N$ is the number density of the obscuring material, $\sigma$ is the material's cross-section, $\kappa$ is the mass extinction coefficient of the material, $l$ is the path length of the absorbing material and $\rho$ is the density of the material. Assuming a specific dust composition, we are left with two free parameters representing the density of the dust and the path length (that is, the thickness of the obscuring structure). Taking the measurements from the same apertures as above (Methods §4), we find that the southern emitting region would need to be obscured by an object with an optical depth of $\tau_{8.7} = 0.41 \pm 0.04$.

The optical depth of such a structure should increase as one gets closer to the SMBH. We measure the average value at 25.1 pc within a 10.1-pc-diameter aperture. Previous measurements[13] at $\lesssim$1 pc give $\tau_{8.7\mu\mathrm{m}} = 0.94$–$1.51$ (their measurement is at a slightly longer wavelength, so we scaled their reported optical depth by a factor 0.74 to compare at 8.7 μm, based on the extinction curve from ref. 58). Assuming a linear change in $\tau$, we obtain an optical depth gradient of $-0.05\ \mathrm{pc^{-1}} \leq \Delta\tau_{8.7\mu\mathrm{m}} \leq -0.02\ \mathrm{pc^{-1}}$.

Since the optical depth $\tau$ is related to dust density, composition and path length through the obscuring material, we explore what a gradient might imply. The dust composition is probably approximately constant, so we focus on dust density and path length. Current disk+wind RT models should naively lead to an increased optical depth at larger radii because the constant-density disk becomes thicker with an opening angle of 5°, leading to a longer path length. However, we observe the opposite trend. The RT modelling in this work assumes a constant dust density in the disk (based on comparisons with Circinus on much smaller scales[12,37]). Our new measurements imply the necessity of a decreasing density gradient counteracting the increase in path length. An exploration of RT parameters would be greatly aided by more constraints on dust temperatures and emission mechanisms, so this will be explored in future work after LBTI observations with more filters have been obtained.

Rearranging equation (2), we find the relation $\rho = \tau_{8.7\mu m}/(l\kappa_{8.7\mu m})$. Because NGC 1068 is inclined ~75° from face on, we can compute an upper limit on the path length ($l$) corresponding to a lower limit on the dust density: $\rho_{lower} = \tau_{8.7\mu m} \sin i/(d\kappa_{8.7\mu m})$. For $i = 75°$, $\kappa_{8.7\mu m} = 12{,}116.5\ m^2\ kg^{-1}$ from ref. 58, $\tau_{8.7\mu m} = 0.41 \pm 0.04$ as above, and $d \approx 25$ pc as measured from the image, we obtain $\rho_{dust} \geq 9 \times 10^{-27}\ g\ cm^{-3}$. The ISM has a mean gas density of 1 atom per cubic centimetre, or $\bar{\rho}_{ISM} = 1.6 \times 10^{-24}\ g\ cm^{-3}$ (ref. 59). This corresponds to a dust-to-gas ratio 25 pc from the AGN of $6 \times 10^{-3}$. This is 0.6 times the mean ISM dust–gas ratio of ~1% (ref. 38). A study of 36 X-ray-observed AGNs yielded dust-to-gas ratios in the range 0.01–1 times the standard ISM value[39]; our measurement falls well within this range.

## Data availability

Raw and processed data corresponding to the current study are available from the corresponding author upon request.

## Code availability

The algorithms used for data processing are described in this work, but data processing Python scripts and data processing instructions are available via GitHub at https://github.com/jwisbell/lbti_fizeau.

## References


1. Antonucci, R. Unified models for active galactic nuclei and quasars. *Annu. Rev. Astron. Astrophys.* **31**, 473–521 (1993).
2. Fabian, A. C. Observational evidence of active galactic nuclei feedback. *Annu. Rev. Astron. Astrophys.* **50**, 455–489 (2012).
3. Wada, K. Radiation-driven fountain and origin of torus around active galactic nuclei. *Astrophys. J.* **758**, 66 (2012).
4. Wada, K., Schartmann, M. & Meijerink, R. Multi-phase nature of a radiation-driven fountain with nuclear starburst in a low-mass active galactic nucleus. *Astrophys. J. Lett.* **828**, L19 (2016).
5. Williamson, D., Hönig, S. & Venanzi, M. 3D radiation hydrodynamics of a dynamical torus. *Astrophys. J.* **876**, 137 (2019).
6. Leftley, J. H. et al. Parsec-scale dusty winds in active galactic nuclei: evidence for radiation pressure driving. *Astrophys. J.* **886**, 55 (2019).
7. Williamson, D., Hönig, S. & Venanzi, M. Radiation hydrodynamics models of active galactic nuclei: beyond the central parsec. *Astrophys. J.* **897**, 26 (2020).
8. Netzer, H. Quasar discs. II—A composite model for the broad-line region. *Mon. Not. R. Astron. Soc.* **225**, 55–72 (1987).
9. Burtscher, L. et al. A diversity of dusty AGN tori. Data release for the VLTI/MIDI AGN Large Program and first results for 23 galaxies. *Astron. Astrophys.* **558**, A149 (2013).
10. López-Gonzaga, N., Burtscher, L., Tristram, K. R. W., Meisenheimer, K. & Schartmann, M. Mid-infrared interferometry of 23 AGN tori: on the significance of polar-elongated emission. *Astron. Astrophys.* **591**, A47 (2016).
11. Isbell, J. W. et al. The dusty heart of Circinus—I. imaging the circumnuclear dust in N-band. *Astron. Astrophys.* **663**, A35 (2022).
12. Isbell, J. W. et al. The dusty heart of Circinus. II. Scrutinizing the LM-band dust morphology using MATISSE. *Astron. Astrophys.* **678**, A136 (2023).
13. Gámez Rosas, V. et al. Thermal imaging of dust hiding the black hole in NGC 1068. *Nature* **602**, 403–407 (2022).
14. GRAVITY Collaborationet al. An image of the dust sublimation region in the nucleus of NGC 1068. *Astron. Astrophys.* **634**, A1 (2020).
15. García-Burillo, S. et al. ALMA resolves the torus of NGC 1068: continuum and molecular line emission. *Astrophys. J. Lett.* **823**, L12 (2016).
16. Impellizzeri, C. M. V. et al. Counter-rotation and high-velocity outflow in the parsec-scale molecular torus of NGC 1068. *Astrophys. J. Lett.* **884**, L28 (2019).
17. García-Burillo, S. et al. ALMA images the many faces of the NGC 1068 torus and its surroundings. *Astron. Astrophys.* **632**, A61 (2019).
18. Gallimore, J. F., Baum, S. A. & O'Dea, C. P. The parsec-scale radio structure of NGC 1068 and the nature of the nuclear radio source. *Astrophys. J.* **613**, 794 (2004).
19. Mutie, I. M. et al. Radio jets in NGC 1068 with e-MERLIN and VLA: structure and morphology. *Mon. Not. R. Astron. Soc.* **527**, 11756–11765 (2024).
20. May, D. & Steiner, J. E. A two-stage outflow in NGC 1068. *Mon. Not. R. Astron. Soc.* **469**, 994–1025 (2017).
21. Hinz, P. M. et al. Overview of LBTI: A Multipurpose Facility for High Spatial Resolution Observations. In *Proc. SPIE 9907, Optical and Infrared Interferometry and Imaging V,* Vol. 990701 (eds Malbet, F. et al.) https://doi.org/10.1117/12.2233795 (SPIE Proceedings, 2016).
22. Ertel, S. et al. Overview and Prospects of the LBTI beyond the Completed HOSTS Survey. In *Proc. SPIE 11446, Optical and Infrared Interferometry and Imaging VII,* Vol. 1144607 (eds Tuthill, P. G. et al.) https://doi.org/10.1117/12.2561849 (SPIE Proceedings, 2020).
23. Leisenring, J. M. et al. Fizeau interferometric imaging of Io volcanism with LBTI/LMIRcam. In *Proc. SPIE 9146, Optical and Infrared Interferometry IV,* Vol. 91462S (eds Rajagopal, J. K. et al.) https://doi.org/10.1117/12.2057290 (SPIE Proceedings, 2014).
24. Conrad, A. et al. Spatially resolved M-band emission from Io's Loki Patera–Fizeau imaging at the 22.8 m LBT. *Astron. J.* **149**, 175 (2015).
25. de Kleer, K. et al. Multi-phase volcanic resurfacing at Loki Patera on Io. *Nature* **545**, 199–202 (2017).
26. Hoffmann, W. F. et al. Operation and performance of the mid-infrared camera, NOMIC, on the Large Binocular Telescope. In *Proc. SPIE 9147, Ground-based and Airborne Instrumentation for Astronomy V,* Vol. 91471O (eds Ramsay, S. K. et al.) https://doi.org/10.1117/12.2057252 (SPIE Proceedings, 2014).
27. Pinna, E. et al. SOUL: The single conjugated adaptive optics upgrade for LBT. In *Proc. SPIE 9909, Adaptive Optics Systems V,* Vol. 99093V (eds Marchetti, E. et al.) https://doi.org/10.1117/12.2234444 (SPIE Proceedings, 2016).
28. Macchetto, F., Capetti, A., Sparks, W. B., Axon, D. J. & Boksenberg, A. HST/FOC imaging of the narrow-line region of NGC 1068. *Astrophys. J. Lett.* **435**, L15 (1994).
29. Bock, J. J. et al. High spatial resolution imaging of NGC 1068 in the mid-infrared. *Astron. J.* **120**, 2904–2919 (2000).
30. Weigelt, G. et al. Diffraction-limited bispectrum speckle interferometry of the nuclear region of the Seyfert galaxy NGC 1068 in the H and K′ bands. *Astron. Astrophys.* **425**, 77–87 (2004).
31. Gallimore, J. F. & Impellizzeri, C. M. V. High-sensitivity observations of the $H_2O$ megamasers of NGC 1068: precise astrometry and detailed kinematics. *Astrophys. J.* **951**, 109 (2023).
32. Leftley, J. H. et al. Chromatically modeling the parsec-scale dusty structure in the center of NGC 1068. *Astron. Astrophys.* **686**, A204 (2024).
33. Vermot, P. et al. Ionized regions in the central arcsecond of NGC 1068. YJHK spatially resolved spectroscopy. *Astron. Astrophys.* **678**, A206 (2023).
34. Barvainis, R. Hot dust and the near-infrared bump in the continuum spectra of quasars and active galactic nuclei. *Astrophys. J.* **320**, 537 (1987).
35. Camps, P. & Baes, M. SKIRT 9: Redesigning an advanced dust radiative transfer code to allow kinematics, line transfer and polarization by aligned dust grains. *Astron. Comput.* **31**, 100381 (2020).
36. Isbell, J. W. et al. Subarcsecond mid-infrared view of local active galactic nuclei. IV. The L- and M-band imaging atlas. *Astrophys. J.* **910**, 104 (2021).
37. Stalevski, M., Tristram, K. R. W. & Asmus, D. Dissecting the active galactic nucleus in Circinus—II. A thin dusty disc and a polar outflow on parsec scales. *Mon. Not. R. Astron. Soc.* **484**, 3334–3355 (2019).

38. Bohlin, R. C., Savage, B. D. & Drake, J. F. A survey of interstellar H I from Lalpha absorption measurements. II. *Astrophys. J.* **224**, 132–142 (1978).
39. Esparza-Arredondo, D. et al. The dust–gas AGN torus as constrained from X-ray and mid-infrared observations. *Astron. Astrophys.* **651**, A91 (2021).
40. Véron-Cetty, M. P. & Véron, P. A catalogue of quasars and active nuclei: 13th edition. *Astron. Astrophys.* **518**, A10 (2010).
41. Cutri, R. M. et al. VizieR Online Data Catalog: AllWISE Data Release (Cutri+ 2013). *VizieR On-line Data Catalog: II/328* (Centre de Données astronomiques de Strasbourg, 2021).
42. Isbell, J. W. et al. The LBTI: Pioneering the ELT era. In *Proc. SPIE 13095, Optical and Infrared Interferometry and Imaging IX,* Vol. 13095 (eds Kammerer, J., Sallum, S. & Sanchez-Bermudez, J.) 1309506 (SPIE Proceedings, 2024); https://doi.org/10.1117/12.3027270
43. Skrutskie, M. F. et al. The Large Binocular Telescope mid-infrared camera (LMIRcam): Final design and status. In *Proc. SPIE 7735, Ground-based and Airborne Instrumentation for Astronomy III,* Vol. 77353H (eds McLean, I. S. et al.) https://doi.org/10.1117/12.857724 (SPIE Proceedings, 2010).
44. Ertel, S., Absil, O., Defrère, D., Augereau, J. C. & Mennesson, B. Prospects for the characterisation of exo-zodiacal dust with the VLTI. *Exp. Astron.* **46**, 401–411 (2018).
45. Leftley, J. H. et al. Resolving the hot dust disk of ESO323-G77. *Astrophys. J.* **912**, 96 (2021).
46. Cruzalèbes, P. et al. A catalogue of stellar diameters and fluxes for mid-infrared interferometry. *Mon. Not. R. Astron. Soc.* **490**, 3158–3176 (2019).
47. Asmus, D., Hönig, S. F., Gandhi, P., Smette, A. & Duschl, W. J. The subarcsecond mid-infrared view of local active galactic nuclei—I. The N- and Q-band imaging atlas. *Mon. Not. R. Astron. Soc.* **439**, 1648–1679 (2014).
48. Leist, M. T. et al. Deconvolution of JWST/MIRI images: applications to an active galactic nucleus model and GATOS observations of NGC 5728. *Astron. J.* **167**, 96 (2024).
49. Conrad, A., Stone, J. & Ertel, S. *Increased Sky Coverage for the 23-Meter LBT* (ONERA, 2023); https://hal.science/hal-04419769
50. Högbom, J. A. Aperture synthesis with a non-regular distribution of interferometer baselines. *Astron. Astrophys. Suppl.* **15**, 417 (1974).
51. Richardson, W. H. Bayesian-based iterative method of image restoration. *J. Opt. Soc. Am.* **62**, 55–59 (1972).
52. Lucy, L. B. An iterative technique for the rectification of observed distributions. *Astron. J.* **79**, 745 (1974).
53. Sanchez-Bermudez, J. et al. *Optical interferometry imaging contest IX*. In *Proc. SPIE 12183, Optical and Infrared Interferometry and Imaging VIII,* Vol. 121831G (eds Mérand, A. et al.) https://doi.org/10.1117/12.2629430 (SPIE Proceedings, 2022).
54. Villar-Martín, M., De Young, D., Alonso-Herrero, A., Allen, M. & Binette, L. Shocks and dust survival in nearby active galaxies: implications for the alignment effect. *Mon. Not. R. Astron. Soc.* **328**, 848–854 (2001).
55. Kraemer, S. B., Ruiz, J. R. & Crenshaw, D. M. Physical conditions in the inner narrow-line region of the Seyfert 2 galaxy NGC 1068. *Astrophys. J.* **508**, 232–242 (1998).
56. Martins, L. P., Rodríguez-Ardila, A., de Souza, R. & Gruenwald, R. Nuclear and extended spectra of NGC 1068—I. Hints from near-infrared spectroscopy. *Mon. Not. R. Astron. Soc.* **406**, 2168–2184 (2010).
57. Kakkad, D. et al. Spatially resolved electron density in the narrow line region of $z$<0.02 radio AGNs. *Astron. Astrophys.* **618**, A6 (2018).
58. Schartmann, M., Meisenheimer, K., Camenzind, M., Wolf, S. & Henning, T. Towards a physical model of dust tori in active galactic nuclei. Radiative transfer calculations for a hydrostatic torus model. *Astron. Astrophys.* **437**, 861–881 (2005).
59. Draine, B. T. *Physics of the Interstellar and Intergalactic Medium* (Princeton Univ. Press, 2011).


## Acknowledgements

V.F.G. acknowledges funding from the National Aeronautics and Space Administration through the Exoplanet Research Program under grant no. 80NSSC21K0394 (principal investigator: S. Ertel). R.G.P., N.M., J. Leftley and P.V. were supported by the French Agence Nationale de la Recherche (ANR) through 'AGN MELBa' grant number ANR-21-CE31-0011.

## Author contributions

J.W.I., J.-U.P., G.W., M.S., J. Leftley, W.J., R.G.P., N.M. and V.G.R. contributed to scientific analysis, modelling and interpretation. J.W.I. and P.V. developed and tested deconvolution methods. J.W.I., S.E., A.B., J.C., V.F.-G., W.F.H., J. Leisenring, J.P. and K.W. took part in observation setup, execution and processing.

## Competing interests

The authors declare no competing interests.

## Additional information

**Extended data** is available for this paper at https://doi.org/10.1038/s41550-024-02461-y.

**Supplementary information** The online version contains supplementary material available at https://doi.org/10.1038/s41550-024-02461-y.

**Correspondence and requests for materials** should be addressed to J. W. Isbell.

**Peer review information** *Nature Astronomy* thanks Santiago Garcia-Burillo and the other, anonymous, reviewer(s) for their contribution to the peer review of this work.

**Reprints and permissions information** is available at www.nature.com/reprints.

**Publisher's note** Springer Nature remains neutral with regard to jurisdictional claims in published maps and institutional affiliations.

Springer Nature or its licensor (e.g. a society or other partner) holds exclusive rights to this article under a publishing agreement with the author(s) or other rightsholder(s); author self-archiving of the accepted manuscript version of this article is solely governed by the terms of such publishing agreement and applicable law.

© The Author(s), under exclusive licence to Springer Nature Limited 2025

[1]Department of Astronomy and Steward Observatory, The University of Arizona, Tucson, AZ, USA. [2]Max-Planck-Institut für Astronomie, Heidelberg, Germany. [3]Large Binocular Telescope Observatory, The University of Arizona, Tucson, AZ, USA. [4]Max-Planck-Institut für Radioastronomie, Bonn, Germany. [5]Astronomical Observatory, Belgrade, Serbia. [6]Sterrenkundig Observatorium, Universiteit Gent, Gent, Belgium. [7]Laboratoire Lagrange, Observatoire de la Côte d'Azur, Université Côte d'Azur, CNRS, Nice, France. [8]Leiden Observatory, Leiden University, Leiden, the Netherlands. [9]LESIA, Observatoire de Paris, Université PSL, CNRS, Sorbonne Université, Université de Paris Cité, Meudon, France. [10]University of California, Santa Cruz, CA, USA. [11]Umweltinstitut München, München, Germany. ✉e-mail: jwisbell@arizona.edu

https://doi.org/10.1038/s41550-024-02461-y

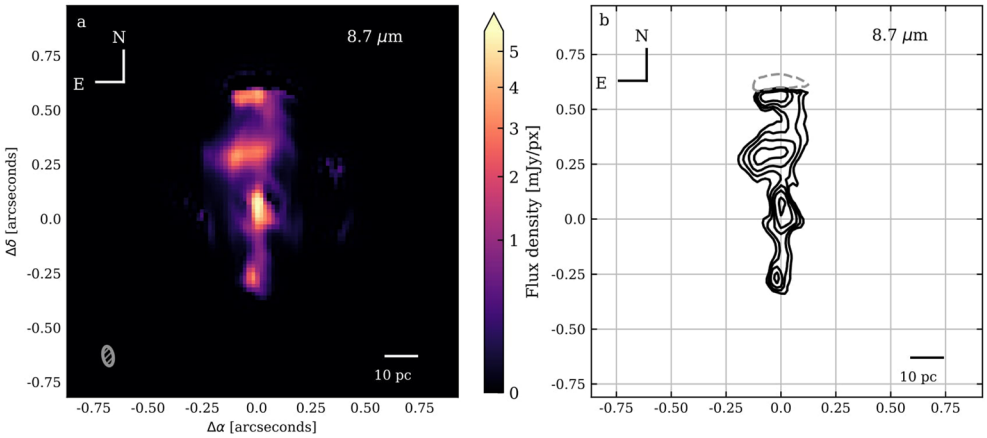


**Extended Data Fig. 1 | LBTI Fizeau image of NGC 1068 after deconvolution using Method 2.** *Panel a)* Deconvolved LBTI Fizeau image of NGC 1068 at 8.7 $\mu$m *Panel b)* The [2, 3, 4, 5, 10, 20, 50] × $\sigma$ contours of the same image. Method 2 used Richardson-Lucy on each observing cycle and then stacking. The results are overall similar to Method 1 (Fig. 2), but with slightly narrower features and a negative flux contour to the north due to a bad pixel channel (visible in Supplementary Figure 2).

https://doi.org/10.1038/s41550-024-02461-y

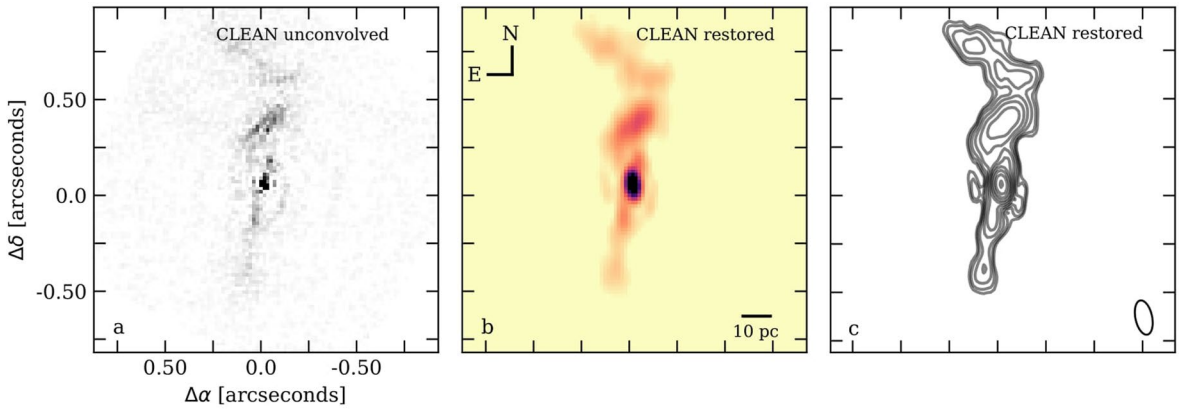


**Extended Data Fig. 2 | Results of the CLEAN- inspired deconvolution algorithm.** *Panel a)* the point source locations produced by the CLEANing iterations. *Panel b)* the CLEAN-inspired image convolved with the restoring beam. *Panel c)* the $[8, 16, 32, 64] \times \sigma$ contours of the restored CLEAN-image, with $\sigma$ measured from the image background. The FWHM of the restoring beam is given in the bottom left corner. Resulting structures resemble those of Fig. 2, albeit with more prominent low-surface-brightness features.

https://doi.org/10.1038/s41550-024-02461-y

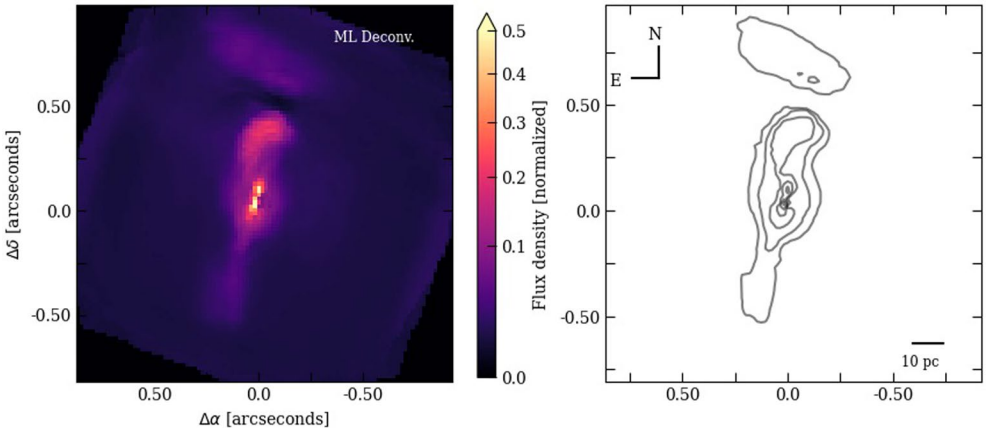


**Extended Data Fig. 3 | Stacked and corotated results of the neural network deconvolution.** *Left)* surface brightness of the recovered emission, normalized to the peak flux. *Right)* Contours of the surface brightness, beginning from 90% of the peak and decreasing by factors of 2 down to a factor 128 below the maximum contour. Low surface brightness features similar to those in Extended Data Fig. 2 are recovered, though the central emission appears to be slightly less extended.

https://doi.org/10.1038/s41550-024-02461-y

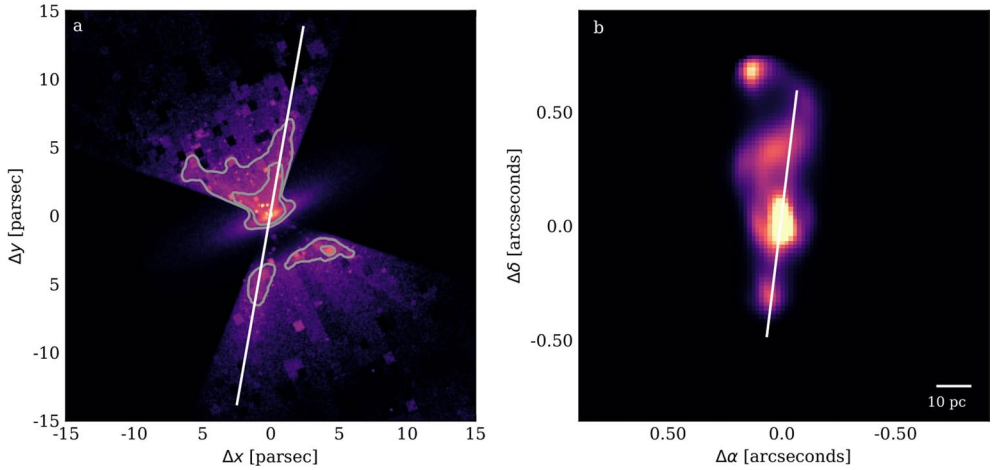


**Extended Data Fig. 4 | Comparison between radiation transfer modeling results and the LBTI observation.** *Left)* Radiation transfer of a disk+wind model. Contours are set at 4, $8 \times 10^{-10}$ W m$^{-2}$sr$^{-1}$ to emphasize the edge- brightening effect and to show that a similar structures to the NEX and southernmost MIR flux we observe are reproduced. *Right)* The same as Fig. 2. In both panels, the white lines represent the extraction aperture used to produce the surface brightness profile in Fig. 4.